Iranian Journal of Science and Technology, Transactions of Civil Engineering (2023) 47:3681–3698
https://doi.org/10.1007/s40996-023-01129-3

RESEARCH PAPER

# Risk Assessment of Three-Dimensional Bearing Capacity of a Circular Footing Resting on Spatially Variable Sandy Soil

**Kouseya Choudhuri[1] · Debarghya Chakraborty[1]**

Received: 30 November 2022 / Accepted: 18 April 2023 / Published online: 7 June 2023


**Abstract**
The present study investigates the probabilistic assessment of the three-dimensional bearing capacity of a circular footing resting on spatially variable sandy soil. The random finite-difference method and Monte Carlo simulation (MCS) technique are utilized to execute all numerical analyses. Three different combinations of friction and dilation angles ($\phi = 30°$, $\psi = 0°$; $\phi = 35°$, $\psi = \phi/6$; and $\phi = 40°$, $\psi = \phi/3$) are considered in this study. The tangent of friction angle ($\tan\phi$) is assumed as the lognormally distributed random field. The variations in mean bearing capacity ($\mu_q$) and failure probability ($p_f$) are presented with respect to normalized horizontal scales of fluctuation ($\theta_x/D = \theta_y/D$) for different friction and dilation angles ($\phi$ and $\psi$), coefficients of variation of $\tan\phi$ ($COV_{\tan\phi}$), normalized vertical scales of fluctuation ($\theta_z/D$), and footing diameters ($D$). The effect of negative cross-correlation between $c$ and $\tan\phi$ is explored. The changes in $p_f$ for different factors of safety ($FOS$), $COV_{\tan\phi}$, and $\theta_x/D = \theta_y/D$ are also illustrated in this study. Based on this observation, the target failure probability ($p_{f\_tgt}$) is plotted against the required factor of safety ($FOS_{req}$). The variations in the allowable bearing capacity ($q_{ad}$) in the design of the footing are also illustrated for different reliability indices ($\beta$), $COV_{\tan\phi}$, and $\theta_x/D = \theta_y/D$.

**Keywords** Circular footing · Bearing capacity · Sandy soil · Spatial variability · Failure probability

## 1 Introduction

The uncertainty associated with geotechnical structures can be broadly classified into three categories: (1) the inherent variability associated with the soil properties, (2) the variability in sampling and testing processes, and (3) the uncertainty related to the model transformation (Phoon and Kulhawy 1999). To incorporate these uncertainties into the structure, engineers have historically used the conventional deterministic-based approach, considering the factor of safety ($FOS$). However, this concept does not ensure that the structure is completely safe against failure, and it often leads to the under-prediction or over-prediction of the responses of the structure (Gong et al. 2015). The rationality of using the failure probability concept in the structure can be justified as it helps in considering the inherent variability associated with the soil parameters using the probabilistic statistics and distribution type of these parameters (Cherubini 2000; Mollon et al. 2009; Nazeeh and Sivakumar Babu 2021; Luo and Luo 2022). The concept of soil spatial variability has been incorporated into several geotechnical problems (Fenton and Griffiths 2002; Griffiths et al. 2002; Griffiths and Fenton 2004; Haldar and Sivakumar Babu 2008; Luo et al. 2012; Kasama and Whittle 2016; Halder and Chakraborty 2020) using the random field theory introduced by Vanmarcke (1983). Several studies on the shallow foundation have taken into account the effect of soil spatial variability (Fenton and Griffiths 2003; Griffiths et al. 2006; Cho and Park 2010; Johari and Sabzi 2017; Wu et al. 2019; Johari et al. 2019; Krishnan and Chakraborty 2022). However, these studies were restricted to two-dimensional strip footings. Reliability-based studies on three-dimensional shallow foundations (e.g., rectangular, square) considering soil spatial variability are limited, as the analyses of these foundations are computationally expensive. Nevertheless, such probabilistic analyses are essential, because these foundations are constructed to carry massive super-structural loads, and the failure associated with them must be appropriately assessed

✉ Debarghya Chakraborty
debarghya@civil.iitkgp.ac.in

Kouseya Choudhuri
kousheyo1995@iitkgp.ac.in

[1] Department of Civil Engineering, Indian Institute of Technology Kharagpur, Kharagpur, West Bengal 721302, India

(Kawa and Puła 2020). Fenton and Griffiths (2005) produced the pioneering work on the probabilistic assessment of individual and two closely spaced square footings considering the spatial variability effect of the elastic modulus to determine the total and differential settlements, respectively. Al-Bittar and Soubra (2014) carried out a reliability-based study on the bearing capacity of square footing, considering cohesion and friction angle as the spatially variable random fields. Ahmed and Soubra (2014) conducted probability-based analyses of a three-dimensional circular footing under inclined loading. Their study aimed to determine the reliability index and the correlated failure modes under ultimate and serviceability limit states. However, the spatial variability effect was not taken into account in their study. Kawa and Pula (2020) studied the spatial variability effect of cohesion and friction angle on the load-carrying capacity of a square footing resting on cohesive-frictional ($c$–$\phi$) soil. The aim of their paper was to study the effect of the horizontal scale of fluctuation on the probabilistic characteristics of the load-carrying capacity. Several other researchers (Simões et al. 2013; Kawa and Puła 2020; Chwała and Kawa 2021) have explored the effect of spatial variability on the three-dimensional bearing capacity of strip footing, considering the modeled length in the out-of-plane direction. Recently, Choudhuri and Chakraborty (2022) conducted probability-based analyses of the three-dimensional bearing capacity of a circular footing resting on a spatially variable two-layer $c$-$\phi$ soil system.

Circular footing on sandy soil is a classical geotechnical problem which has been used worldwide over the decades. Several researchers (Manoharan and Dasgupta 1995; Erickson and Drescher 2002; Loukidis and Salgado 2009) have conducted deterministic analyses on the bearing capacity of circular footing on sandy soil, exploring the effect of both associativity and non-associativity. Erickson and Drescher (2002) carried out a two-dimensional axisymmetric analysis of a circular footing having $D = 12$ m for $\phi = 20°$, 35°, 40°, and 45° and corresponding $\psi = 0°$, $\phi/2$, and $\phi$, considering mass density ($\rho_m$) = 1500 kg/m$^3$, cohesion ($c$) = 0.1 kPa and $\rho_m = 2500$ kg/m$^3$, $c = 100$ kPa. The ultimate bearing capacity of the circular footing was found to increase with the increase in dilation angle for a particular $\phi$ value. Ornek et al. (2012) carried out a numerical study using finite-element software to predict the scale effect of circular footing supported by partially replaced granular fill on natural clay deposits. A two-dimensional axisymmetric model was generated in their study, and the numerical analysis results were validated with small-scale field tests. It was observed that the ultimate bearing capacity increased with the increase in footing diameter. The present study compares the results obtained by Erickson and Drescher (2002) for the cases of $\phi = 20°$, 35°, and 40° and corresponding $\psi = 0°$, $\phi/2$, and $\phi$, considering $\rho_m = 1500$ kg/m$^3$, and $c = 0.1$ kPa, and the comparison is presented in Table 1. Similarly, this study compares the field test results obtained by Ornek et al. (2012), considering the diameter of the footing, $D = 0.12$ m, and the thickness of the granular layer, $H_{gr} = 0.333D$. The comparison is illustrated in Fig. 1. It can be seen that the results obtained from the present study closely resemble those in the literature.

From the extensive literature survey, it is found that no reliability-based study is available on the three-dimensional circular surface footing resting on sandy soil, considering the spatial variability effect of the soil friction angle. Hence, the present study tries to provide a general perspective of the problem. The primary objective of this paper is to study the variations in $\mu_q$ and $p_f$ of the system for different $\theta_x/D = \theta_y/D$. In this study, the friction angle ($\phi$) is characterized as the

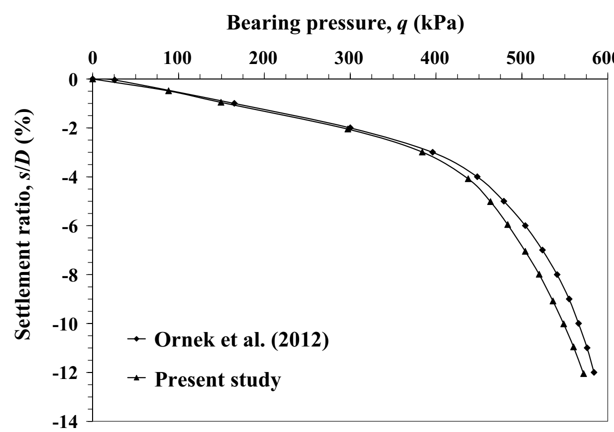


**Fig. 1** Comparison of bearing pressure versus settlement ratio curve for the circular footing between the present study and Ornek et al. (2012)

**Table 1** Comparison of $q_{ud}$ (in kPa) of circular footing between the present study and Erickson and Drescher (2002)

| $\phi$ | Erickson and Drescher (2002)[a] | | | Present study[b] | | |
|---|---|---|---|---|---|---|
| | $\psi = 0°$ | $\psi = \phi/2$ | $\psi = \phi$ | $\psi = 0°$ | $\psi = \phi/2$ | $\psi = \phi$ |
| 20° | 242 | 265 | 271 | 251.5 | 258.7 | 270.5 |
| 35° | 3140 | 4045 | 4330 | 3267.7 | 4109 | 4450 |
| 40° | 6903 | 11,150 | 12,800 | 6968.3 | 11,569.9 | 13,057 |

[a]Axisymmetric model in FLAC$^{2D}$

[b]Three-dimensional model in FLAC$^{3D}$

spatially variable random field. Since the dilation angle ($\psi$) is assumed to be the function of friction angle, it is also simulated as the random field. The soil cohesion is assumed to be a non-random parameter in the study. However, the effect of cross-correlation between cohesion and friction angle ($\rho_{c\text{-}\tan\phi}$) is also explored in the present study as a representative case where the soil cohesion is characterized as a random field. The changes in $p_f$ for different $FOS$ and $\theta_x/D = \theta_y/D$ are explored in the study. Design charts are provided, illustrating the variations in the $FOS_{req}$ for different $p_{f\_tgt}$. The $q_{ad}$ of the footing is evaluated based on a few standard reliability indices ($\beta$), and the variations in $q_{ad}$ are also shown for different coefficients of variation of tan ($COV_{\tan\phi}$) and $\theta_x/D = \theta_y/D$.

## 2 Details of Finite-Difference Numerical Modeling

A three-dimensional rigid circular footing with a rough base placed on the surface of sandy soil is represented by a schematic diagram shown in Fig. 2a. The diameter of the footing is represented by $D$. FLAC$^{3D}$ software (Itasca 2012) is used to model the footing and the soil domain and to execute all the numerical analyses. In the probabilistic analysis, a full model domain is considered where the stretch of the model domain in both horizontal directions is assumed to be 10$D$, whereas the stretch of the model in the vertical direction is considered to be 5$D$. The model domain is chosen after several trials to avoid boundary effects. The horizontal and vertical movements are restricted at the bottom boundary, whereas only the vertical movement is allowed at the outer side boundaries by the provision of the lateral restriction. Radially graded mesh around a cylindrical tunnel with a solid core is incorporated for discretization of the soil domain. Finer mesh is generated adjacent to the footing area where the high-stress gradient is expected, whereas the mesh size becomes coarser as it approaches the boundary. Total elements of the domain are selected as 18,144 to maintain the balance between efficiency and accuracy. The finite-difference discretized mesh is shown in Fig. 2b. The sandy soil is assumed to obey the elastic-perfectly plastic Mohr–Coulomb yield criterion. Three different friction angles ($\phi = 30°$, 35°, and 40°) are considered in the present study. As per Sloan (2013), the $\psi$ of the soil varies from 0° to $\phi$/3. Hence, three different dilation angles, $\psi = 0°$, $\phi$/6, and $\phi$/3, are considered in this study to correspond to $\phi = 30°$, 35°, and 40°, respectively. Young's modulus ($E$) and Poisson's ratio ($\upsilon$) of the soil are assumed to be 30 MPa and 0.3, respectively (as per Johari and Sabzi 2017). After mesh generation and allocation of soil properties to all the elements, the whole model is analyzed under gravity loading. The footing roughness is ensured by providing lateral resistance to the footing nodes.

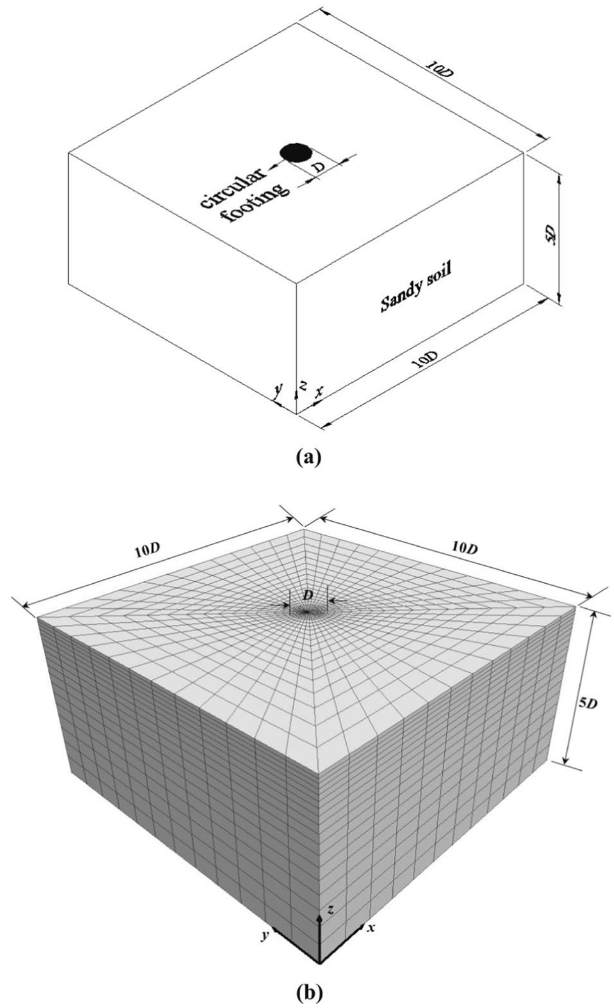


**Fig. 2** Circular footing on sandy soil: **a** schematic diagram, **b** finite-difference discretization

An optimum and very small amount of controlled downward displacement of magnitude $5 \times 10^{-6}$ m (per step) is applied at the specified nodes. Then the model undergoes a certain number of steps until the limiting value of bearing capacity is achieved (Halder and Chakraborty 2020; Kawa and Puła 2020). It should be noted that a small amount of cohesion ($c = 0.5$ kPa) is considered in all the analyses to achieve numerically stable results. For this reason, the results are presented using the ultimate bearing capacity of footing ($q_u$) instead of the bearing capacity factor, $N_\gamma$.

## 3 Deterministic Analysis

Deterministic analyses are carried out for three different combinations of friction and dilation angles (i.e., $\phi = 30°$, $\psi = 0°$; $\phi = 35°$, $\psi = \phi/6$; and $\phi = 40°$, $\psi = \phi/3$) and three different diameters ($D = 0.5$ m, 1 m, and 2 m) of the circular footing. The importance of deterministic analyses is justified as the results obtained can be used as a reference to calculate the $p_f$ of the system. Both $\phi$ and $\psi$ are considered to be spatially constant during the deterministic analyses. The bearing pressure–settlement ratio ($q$ versus $s/D$) curves for three different $\phi$, $\psi$, and $D$ are illustrated in Fig. 3a, b, and c. The bearing capacity of the footing increases with the increase in $\phi$ and $\psi$, which is a very intuitive observation. In the present study, the $q_{ud}$ of the footing is expressed as the footing pressure for a particular settlement ratio ($s/D$) of 6%. However, in the case of $\phi=40^{\text{o}}$, $\psi=\phi/3$ for $D=0.5$ m and 1 m, and for all the combinations of $\phi$ and $\psi$ for $D=2$ m, the stable value of footing pressure has yet to be reached. According to Eurocode 7 (CEN 2013), the permissible settlement of a typical footing for a normal residential building can be considered as 75–135 mm, and the settlement value of 6% of $D$ (even for $D=2$ m) falls within this range. Hence, the $q_{ud}$ of the footing is defined based on the settlement criterion. The $q_{ud}$ of the footing corresponding to $s/D=6\%$ for different $\phi$, $\psi$, and $D$ is shown in Fig. 3d, where it is observed that the $q_{ud}$ of the footing (at $s/D=6\%$) increases as the footing diameter increases, irrespective of the change in $\phi$ and $\psi$.

## 4 Probabilistic Analyses

### 4.1 Random Fields for $\phi$ and $\psi$

Generally, soil is highly complex in nature, depending on its mineralogical components, physicomechanical behavior, and loading history. Hence, layer-wise variations in soil properties may be observed in nature, in which the variation can also be observed within a single layer of soil (Johari et al. 2017). In the present study, $\phi$ is characterized by a random field. Since the dilation angle for $\phi=35°$ and 40° is a function of $\phi$, the dilation angles for these two friction angles can also be defined by the random fields. However, due to the very small cohesion value (i.e., $c=0.5$ kPa), it is considered homogeneous throughout the study. Similarly, this study considers $E$ and $\upsilon$ as spatially constant. The random

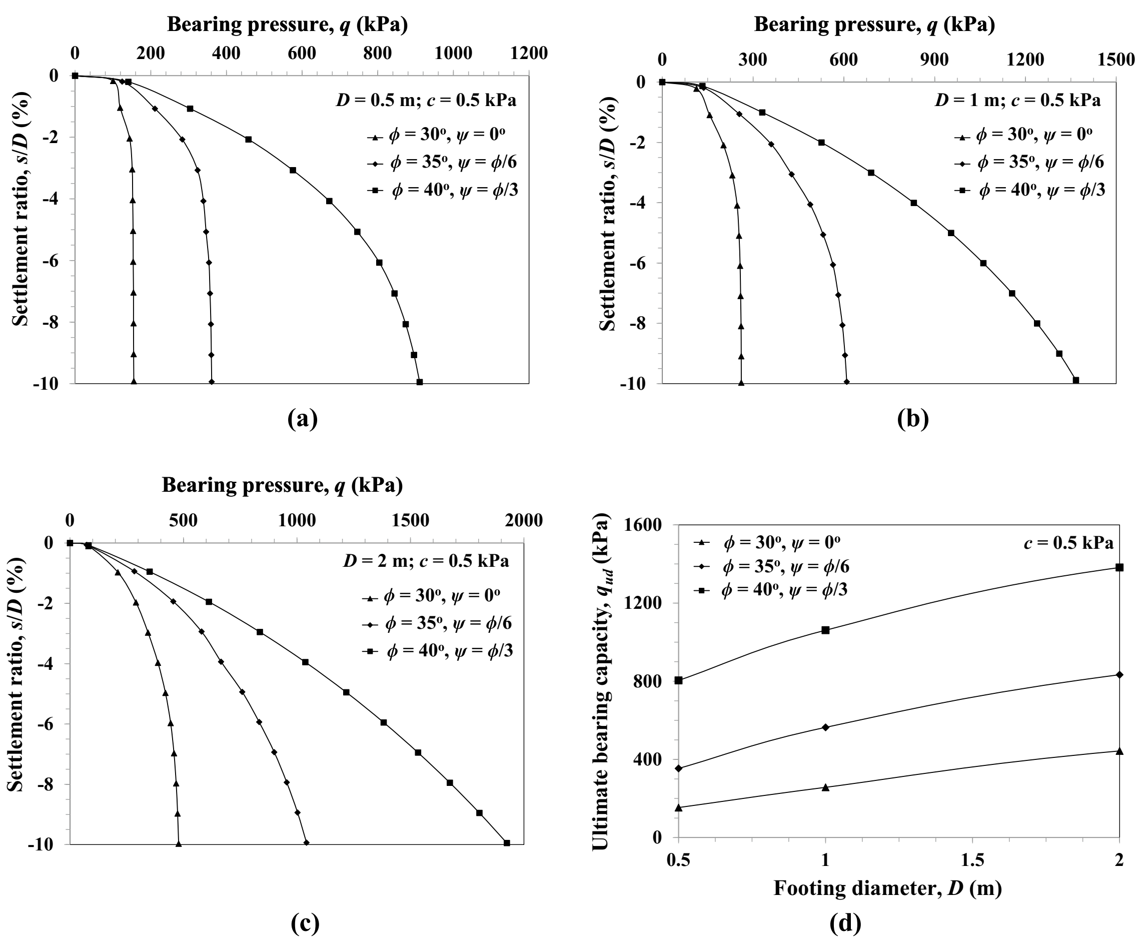


**Fig. 3** Bearing pressure versus settlement ratio curves for circular footing with **a** $D=0.5$ m, **b** $D=1$ m, **c** $D=2$ m, and **d** variation in $q_{ud}$ with respect to $D$ corresponding to $s/D=6\%$

field for tan$\phi$ is assumed to be lognormally distributed, as it always gives non-negative random numbers. The tan$\phi$ is chosen as a random field instead of $\phi$, as it ensures that the randomly initiated $\phi$ values are between 0° and 90° (Griffiths et al. 2011; Krishnan and Chakraborty 2022).

In the present study, a three-dimensional Markov exponential autocorrelation function, $\rho(\varsigma)$ , is used to define the correlation structure of the randomly generated friction field. The three-dimensional Markov function uses the scales of fluctuation (SOFs) in both the horizontal ($\theta_x$, $\theta_y$) and vertical ($\theta_z$) directions and can be expressed as follows:

$$\rho(\varsigma_x, \varsigma_y, \varsigma_z) = \exp\left(\frac{-2|\varsigma_x|}{\theta_x} + \frac{-2|\varsigma_y|}{\theta_y} + \frac{-2|\varsigma_z|}{\theta_z}\right) \tag{1}$$

In the above equation, $\varsigma_x = (x_k - x_l)$, $\varsigma_y = (y_k - y_l)$, and $\varsigma_z = (z_k - z_l)$ are the centroidal distances between the $k$th and $l$th elements, where $k = 1, 2, 3, \ldots, E_n$, and $l = 1, 2, 3, \ldots, E_n$ ($E_n$ is the total number of elements in the generated mesh). $\theta_x$, $\theta_y$, and $\theta_z$ are the SOFs in the $x$, $y$, and $z$ directions, respectively. The SOF defines the distance over which the randomly generated values of a soil parameter are strongly correlated with each other. Lower SOF values define ragged fields, whereas higher SOF values define smoothly varying random fields (Griffiths et al. 2002). The present study considers the SOFs in the $x$ and $y$ directions as equal (i.e., $\theta_x = \theta_y$), following the literature (Kawa and Puła 2020; Choudhuri and Chakraborty 2021). Considering the soil deposition process in nature, $\theta_x = \theta_y$ is generally assumed to be greater than $\theta_z$ (Jamshidi Chenari and Mahigir 2014). Hence, the anisotropic random field is considered in the present study where $\theta_x = \theta_y > \theta_z$. However, it should be noted that there are a few cases where $\theta_z$ is considered to be greater than $\theta_x = \theta_y$ to explore the effect of $\theta_z$ on the probabilistic characteristics of bearing capacity. The parameters used in the probabilistic study are outlined in Table 2.

The spatially variable random field of $\phi$ is generated using the Cholesky decomposition method (Haldar and Sivakumar Babu 2008; Kasama and Whittle 2016). Since the obtained autocorrelation matrix $\rho(\varsigma)$ is positive definite, the matrix can be factorized into the lower triangular matrix ($Q$) and its transpose ($Q^T$), as follows:

$$\rho(\varsigma) = QQ^{\mathrm{T}} \tag{2}$$

The spatially correlated standard normal random field for friction angle $\left(G_{\ln\tan\overline{\phi}}\right)$ can be evaluated using the lower triangular matrix ($Q$) as follows:

$$G_{\ln\tan\overline{\phi}} = \sum_{j=1}^{i} Q_{ij}(G_{\ln\tan\phi})_j, i = 1, 2, 3, \ldots, E_n \tag{3}$$

where $G_{\ln\tan\phi}$ denotes the column vector of the uncorrelated standard normal variable with zero mean and unit standard deviation. As tan$\phi$ of the soil is assumed to be lognormally distributed, the spatially varied random fields for $\phi$ can be expressed as follows:

$$\phi(\xi) = \tan^{-1}[\exp\{\mu_{\ln\tan\phi} + \sigma_{\ln\tan\phi}G_{\ln\tan\overline{\phi}}\}] \tag{4}$$

In the above equation, $\xi = \xi(x, y, z)$ denotes the spatial location of a point where the friction field is required. The underlying normal distribution parameters $\mu_{\ln\tan\phi}$ and $\sigma_{\ln\tan\phi}$ are evaluated using the following transformations:

$$\sigma^2_{\ln\tan\phi} = \ln\left(1 + \frac{\sigma^2_{\tan\phi}}{\mu^2_{\tan\phi}}\right) = \ln(1 + \mathrm{COV}^2_{\tan\phi}) \tag{5}$$

$$\mu_{\ln\tan\phi} = \ln\mu_{\tan\phi} - \frac{1}{2}\sigma^2_{\ln\tan\phi} \tag{6}$$

To extract the centroidal coordinates of all the elements of the discretized mesh as a text file, an in-house FISH subroutine is written in FLAC$^{3D}$. After extracting those coordinates into the text files, the files are loaded into MATLAB (The MathWorks Inc. 2020). The spatially varied random fields for $\phi$ and $\psi$ are generated in MATLAB using the parameters provided in Table 2. Then the obtained random fields are taken back to FLAC$^{3D}$ as the text file and assigned to each

**Table 2** Parameters used in probabilistic analyses

| | |
|---|---|
| *Fixed parameters* | |
| Cohesion, $c$ (kPa) | 0.5 |
| Normalized horizontal scales of fluctuation, $\theta_x/D = \theta_y/D$ | 1.25, 2.5, 5, 10 |
| Number of Monte Carlo realizations | 300 |
| *Variable parameters* | |
| Mean of tan$\phi$ ($\mu_{\tan\phi}$) and dilation angle ($\psi$) | tan(30°) ($\psi = 0°$), tan(35°) ($\psi = \phi/6$), tan(40°) ($\psi = \phi/3$) ($COV_{\tan\phi} = 20\%$, $D = 1$ m, $\theta_z/D = 1$) |
| Coefficients of variation of the tangent of friction angle, $COV_{\tan\phi}$ | 5%, 10%, 20% ($\mu_{\tan\phi} = \tan(30°)$, $\psi = 0°$, $D = 1$ m, $\theta_z/D = 1$) |
| Normalized vertical scales of fluctuation, $\theta_z/D$ | 1, 2, 4, 8 ($\mu_{\tan\phi} = \tan(35°)$, $\psi = \phi/6$, $COV_{\tan\phi} = 20\%$, $D = 1$ m, $\theta_x/D = 1$) |
| Footing diameter, $D$ | 0.5 m, 1 m, 2 m ($\mu_{\tan\phi} = \tan(30°)$, $\psi = 0°$, $COV_{\tan\phi} = 20\%$, $\theta_z/D = 1$) |

element of the discretized mesh using the FISH subroutine. The exemplary random fields for different $\phi$ for the constant values of $\theta_x/D = \theta_y/D$, $\theta_z/D$, $COV_{\tan\phi}$, and $D$ are illustrated in Fig. 4. Cross-sectional views of the friction field along the centroid of the footing are also depicted in that figure. It should be noted that the illustrated fields correspond to a particular Monte Carlo realization. The $\mu_q$ and $COV_q$ of $q_u$ for the given sets of probabilistic parameters are evaluated

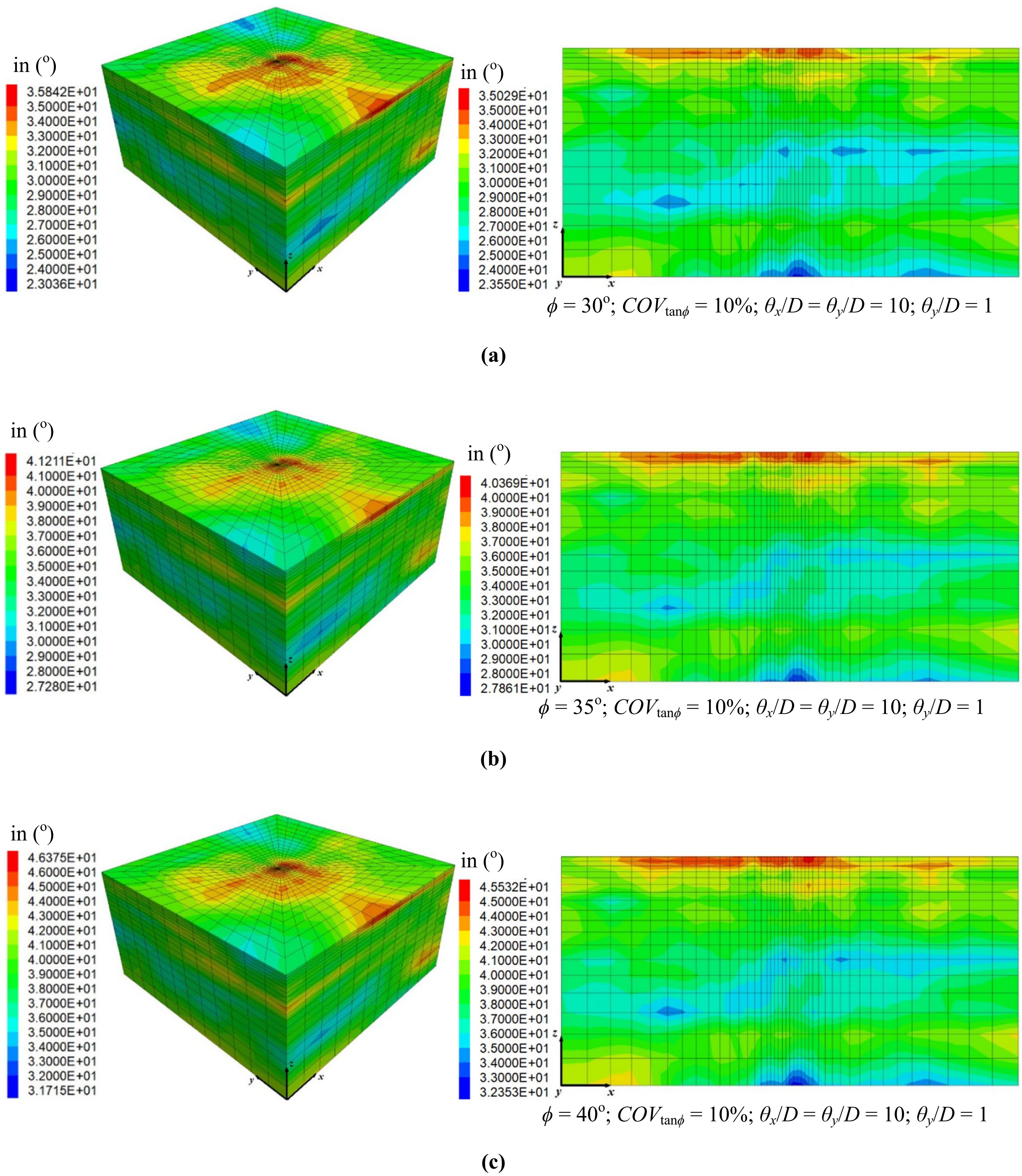


**Fig. 4** Spatially variable random fields of friction angle ($\phi$) for **a** $\phi = 30°$, **b** $\phi = 35°$, and **c** $\phi = 40°$

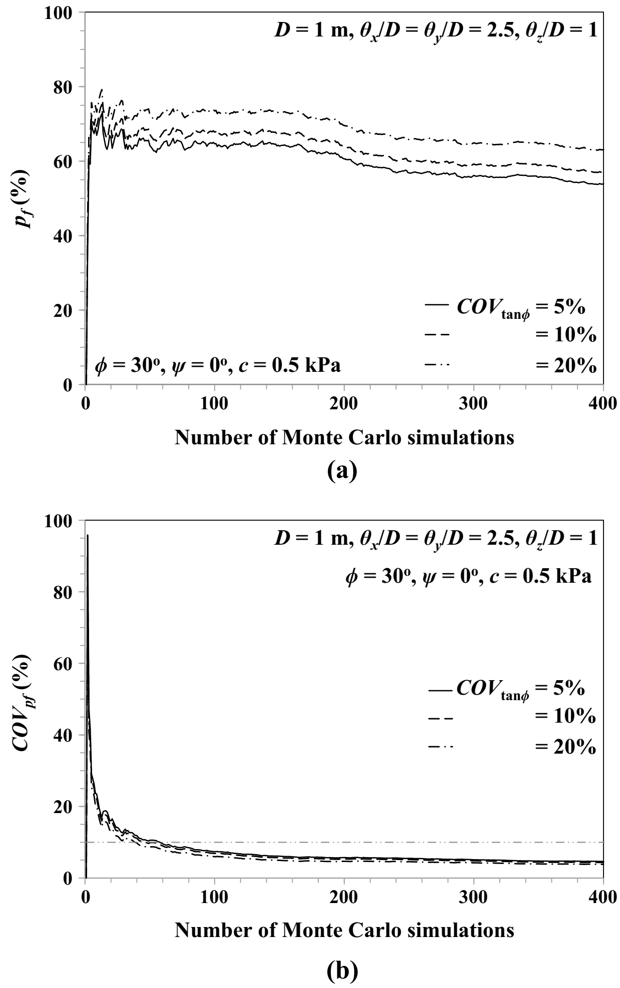


**Fig. 5** Variations in **a** $p_f$ and **b** $COV_{pf}$ of the footing with respect to MCS for different $COV_{\tan\phi}$

using the Monte Carlo simulation (MCS) technique. In addition, the probabilistic $q_u$ is evaluated at $s/D = 6\%$. The coefficient of variation of the failure probability ($COV_{pf}$) of the footing is evaluated to check the performance of the MCS (Cheng et al. 2018). This is essential, because as the number of MCS increases, the numerical accuracy increases. However, the probabilistic analyses of the three-dimensional problem under the MCS framework require substantial computational effort. Hence, a trade-off between the computational efficiency and accuracy of the obtained solution should be established. Following the central limit theorem, the estimated $p_f$ can be used to determine the accuracy of the chosen MCS. The $COV_{pf}$ is evaluated using the following equation:

$$\mathrm{COV}_{pf} = \sqrt{\frac{1 - p_{\mathrm{f}}}{N_{\mathrm{mcs}} p_{\mathrm{f}}}} \tag{7}$$

In the above equation, $N_{\mathrm{mcs}}$ denotes the number of Monte Carlo simulations. As per the literature (Cheng et al. 2018), the reasonable value of the $COV_{pf}$ can be set as 10%. The variations in $p_f$ and $COV_{pf}$ for different MCS and $COV_{\tan\phi}$ are illustrated in Fig. 5. It is observed that the $p_f$ of the system is almost stable after 300 Monte Carlo realizations. The obtained $COV_{pf}$ values for different $COV_{\tan\phi}$ are also well below 10% after the 300 MC realizations. Hence, all the probabilistic analyses are carried out for the 300 MC realizations. All analyses were performed on a PC with 12 GB RAM and a single Intel Core i5 processor with a clock speed of 1.80 GHz, and around 22 h of computational time was required to complete the 300 MCSs for a particular set of probabilistic input statistics.

## 4.2 Failure Probability

A footing is said to fail under the ultimate limit state of collapse when the stress applied to the footing (i.e., $q_{app}$) exceeds the $q_u$ of the underlying soil. Following the existing literature (Griffiths et al. 2002; Haldar and Sivakumar Babu 2008; Krishnan and Chakraborty 2022), the present study considers the $q_{ud}$ as the stress applied to the footing. Since $\tan\phi$ is assumed to be lognormally distributed, the distribution of the probabilistic ultimate bearing capacity ($q_u$) will most likely follow the lognormal distribution. However, the actual distribution of $q_u$ is compared with the assumed hypothetical cumulative lognormal distribution having the parameters $\mu_q$ and $COV_q$ (Fig. 6a). The plot is constructed for the case of $\phi = 30^{\circ}$, $\psi = 0^{\circ}$, $D = 1$, $\theta_x/D = \theta_y/D = 2.5$, $\theta_z/D = 1$, and $COV_{\tan\phi} = 20\%$. The observed distribution of $q_u$ closely matches the theoretical distribution. The distribution of $q_u$ is further confirmed using the Kolmogorov–Smirnov test (Massey 1951), which is performed for three different significance levels (i.e., $\alpha = 1\%$, 5%, and 20%). For each significance level, the maximum absolute difference between the actual and theoretical distribution is well below the critical value. Thus, the lognormal distribution is acceptable at the given significance levels. Along with this cumulative distribution function (*CDF*) plot, the actual distribution of $q_u$ is expressed through the histogram illustrated in Fig. 6b. It is observed that the histogram of $q_u$ closely resembles the lognormal fit. Hence, the $p_f$ of the system can be estimated as the probability for which the evaluated $q_u$ is less than the $q_{ud}$, as follows:

$$p_{\mathrm{f}} = P(q_u < q_{\mathrm{app}}) = P(q_u < q_{\mathrm{ud}}) = \Phi\left(\frac{\ln(q_{\mathrm{ud}}) - \mu_{\ln q_u}}{\sigma_{\ln q_u}}\right) = \Phi(-\beta) \tag{8}$$

where $\Phi(.)$ is the cumulative normal distribution function. $\mu_{\ln q_u}$ and $\sigma_{\ln q_u}$ are the transformed normal distribution

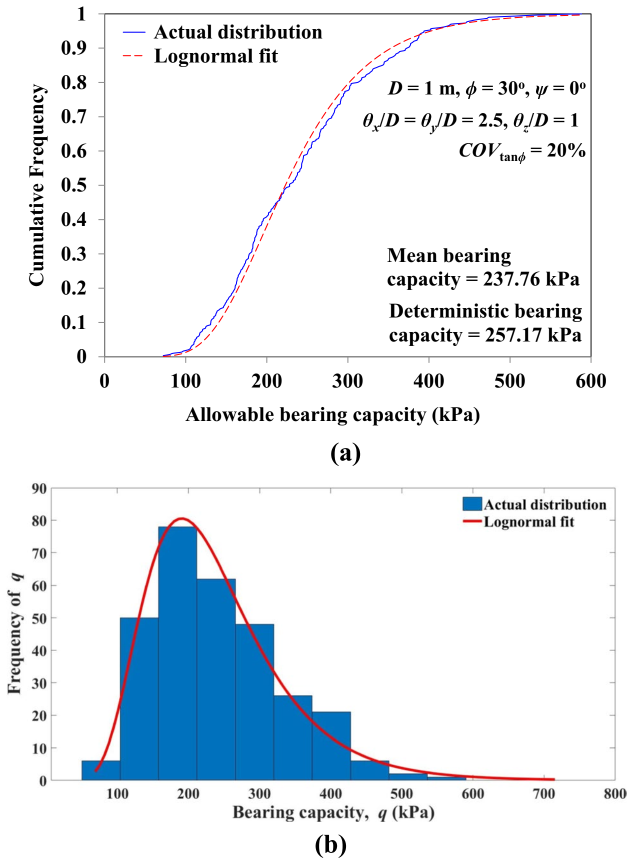


**Fig. 6** a Comparison of actual distribution with the assumed theoretical lognormal distribution of $q_u$, **b** histogram of $q_u$ with lognormal fit for $D=1$ m, $\phi=30°$, $\psi=0°$, $c=0.5$ kPa, $COV_{\tan\phi}=20\%$, $\theta_x/D=\theta_y/D=2.5$, and $\theta_z/D=1$

parameters, and $\beta$ defines the reliability index. It should be noted that in this section, the obtained $p_f$ is for $FOS=1$.

## 5 Results Obtained from the Probabilistic Analyses

This section is devoted to the detailed discussion on the variation in $\mu_q$ and $p_f$ with respect to different $\theta_x/D=\theta_y/D$. The effect of $\theta_z/D$ on $\mu_q$ and $p_f$ is also scrutinized in this section for the particular values of $\phi$ and $\psi$, $COV_{\tan\phi}$, and $D$. The next sub-section illustrates the failure mechanism of the spatially variable random soil under the footing for different $\phi$ and $\psi$. Then, the changes in $CDF$ and $PDF$ of $q_u$ for different $COV_{\tan\phi}$, $\theta_x/D=\theta_y/D$, and $\theta_z/D$ are discussed. The impacts of different $FOS$ on the $p_f$ for different $COV_{\tan\phi}$ and $\theta_x/D=\theta_y/D$ are also discussed in this section, and based on this, the plots of $p_{f\_tgt}$ versus $FOS_{req}$ are provided for different $COV_{\tan\phi}$ and $\theta_x/D=\theta_y/D$. Finally, the $q_{ad}$ of the footing is evaluated for different $\beta$, $COV_{\tan\phi}$, and $\theta_x/D=\theta_y/D$.

### 5.1 Variations in $\mu_q$ and $p_f$ for Different $\theta_x/D=\theta_y/D$, $\phi$, and $\psi$

The variations in $\mu_q$ for different $\theta_x/D=\theta_y/D$, $\phi$, and $\psi$ with constant values of $D=1$ m, $COV_{\tan\phi}=20\%$, and $\theta_z/D=1$ are illustrated in Fig. 7a. Similarly, the variations in $p_f$ for the same set of parameters are shown in Fig. 7e. For $\phi=30°$, $\psi=0°$ and $\phi=35°$, $\psi=\phi/6$, the $\mu_q$ increases as $\theta_x/D=\theta_y/D$ increases, whereas for $\phi=40°$, $\psi=\phi/3$, $\mu_q$ decreases with an increase in $\theta_x/D=\theta_y/D$. However, the variation in $\mu_q$ with respect to $\theta_x/D=\theta_y/D$ is restricted to a very small

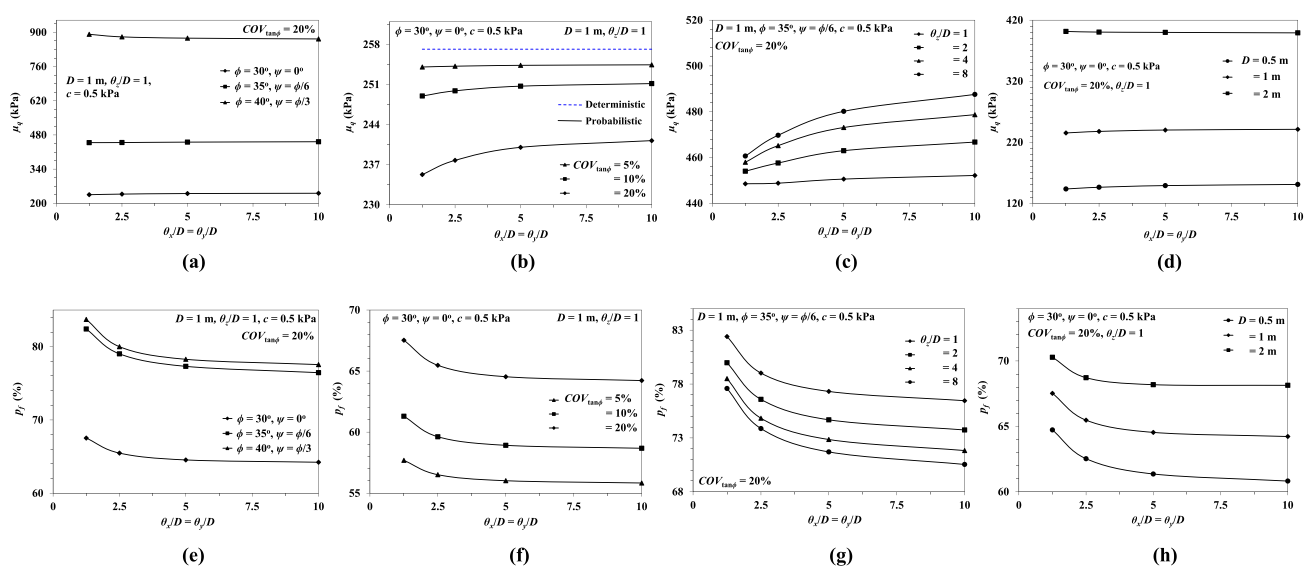


**Fig. 7** Variations in $\mu_q$ with respect to $\theta_x/D=\theta_y/D$ corresponding to different **a** $\phi$ and $\psi$, **b** $COV_{\tan\phi}$, **c** $\theta_z/D$ and **d** $D$; variations in $p_f$ with respect to $\theta_x/D=\theta_y/D$ corresponding to different **e** $\phi$ and $\psi$, **f** $COV_{\tan\phi}$, **g** $\theta_z/D$, and **h** $D$

range. The $p_f$ of the system decreases with the increase in $\theta_x/D = \theta_y/D$ irrespective of the change in magnitude of $\phi$ and $\psi$. For a particular value of $\theta_x/D = \theta_y/D$, the $p_f$ of the system increases remarkably as $\phi$ increases from 30° to 35°, and $\psi$ increases from 0° to $\phi$/6. However, a marginal increase in $p_f$ is observed as $\phi$ increases from 35° to 40°, and $\psi$ increases from $\phi$/6 to $\phi$/3. It is also observed that the rate of change in both $\mu_q$ and $p_f$ with respect to $\theta_x/D = \theta_y/D$ decreases as $\theta_x/D = \theta_y/D$ increases. Halder and Chakraborty (2020) and Kawa and Pula (2020) reported a similar observation.

### 5.2 Variations in $\mu_q$ and $p_f$ for Different $\theta_x/D = \theta_y/D$ and $COV_{\tan\phi}$

Figure 7b and f illustrate the variations in $\mu_q$ and $p_f$, respectively, for different $\theta_x/D = \theta_y/D$ and $COV_{\tan\phi}$ corresponding to the constant values of $\phi = 30°$, $\psi = 0°$, $D = 1$ m, and $\theta_z/D = 1$. The $\mu_q$ of the footing decreases as the $COV_{\tan\phi}$ increases, whereas the $p_f$ increases with an increase in $COV_{\tan\phi}$. These observations can be attributed to the increase in the randomness of generated $\phi$ values with the increase in $COV_{\tan\phi}$. Hence, the chances of producing weaker strength zones under the footing increase as the $COV_{\tan\phi}$ increases, which leads to failure of the soil under the footing when the load is applied to the footing. It is also observed that the rate of change in $\mu_q$ with respect to $\theta_x/D = \theta_y/D$ decreases as the $COV_{\tan\phi}$ decreases.

### 5.3 Variations in $\mu_q$ and $p_f$ for Different $\theta_x/D = \theta_y/D$ and $\theta_z/D$

Figure 7c and g illustrate the variations in $\mu_q$ and $p_f$, respectively, for different $\theta_x/D = \theta_y/D$ and $\theta_z/D$ corresponding to the constant values of $\phi = 35°$, $\psi = \phi/6$, $COV_{\tan\phi} = 20\%$, and $D = 1$ m. The $\mu_q$ and $p_f$ of the system increase and decrease, respectively, as $\theta_z/D$ increases, irrespective of $\theta_x/D = \theta_y/D$. Krishnan and Chakraborty (2022) reported a similar observation when the mean bearing capacity factor ($\mu N_\gamma$) is varied with $\theta_z/D$. Similarly, for each set of $\theta_z/D$, the $\mu_q$ of the system increases as $\theta_x/D = \theta_y/D$ increases. However, the $p_f$ of the system decreases as $\theta_x/D = \theta_y/D$ increases.

### 5.4 Variations in $\mu_q$ and $p_f$ for Different $\theta_x/D = \theta_y/D$ and $D$

Figure 7d and h illustrate the variations in $\mu_q$ and $p_f$, respectively, for different $\theta_x/D = \theta_y/D$ and $D$ corresponding to constant values of $\phi = 30°$, $\psi = 0°$, $COV_{\tan\phi} = 20\%$, and $\theta_z/D = 1$. For $D = 0.5$ m and 1 m, the $\mu_q$ of the system increases as $\theta_x/D = \theta_y/D$ increases, whereas for $D = 2$ m, $\mu_q$ decreases as $\theta_x/D = \theta_y/D$ increases. In the case of $p_f$, it increases with the increase in $D$ for constant values of $\theta_x/D = \theta_y/D$. However, the $p_f$ of the system decreases as $\theta_x/D = \theta_y/D$ increases, irrespective of the change in $D$. It should be noted that the results obtained for different $D$ are based on non-dimensionalized parameters such as $\theta_x/D = \theta_y/D$ and $\theta_z/D$, and the domain of the model is also considered based on the footing diameter. Hence, a particular value of $\theta_x/D = \theta_y/D$ and $\theta_z/D$ provides the different values of $\theta_x = \theta_y$ and $\theta_z$ for different $D$, which can be attributed to the decreasing trend of $\mu_q$ with respect to $\theta_x/D = \theta_y/D$ for $D = 2$ m.

### 5.5 Effect of Cross-Correlation Between $c$ and $\tan\phi$

The soil shear strength parameters (i.e., $c$ and $\phi$) show the degree of interdependence between them. The present study considers the cross-correlation between $c$ and $\tan\phi$ instead of $\phi$, and it is represented as the cross-correlation coefficient $\rho_{c\text{-}\tan\phi}$. For this reason, the soil cohesion is characterized as the lognormally distributed random field with a mean ($\mu_c$) = 0.5 kPa and coefficient of variation ($COV_c$) = 50%. In general, the soil cohesion and friction angle are negatively correlated, and the cross-correlation coefficient varies from −0.70 to −0.24 (Cherubini 2000; Johari et al. 2017). The typical value of $\rho_{c\text{-}\tan\phi}$ is considered as −0.5 for this study following Johari et al. (2017), to generate the cross-correlated random fields for $c$ and $\tan\phi$. The obtained $\mu_q$ and $p_f$ of the system for $\rho_{c\text{-}\tan\phi} = -0.5$ are compared with the results for $\rho_{c\text{-}\tan\phi} = 0$.

The cross-correlation between $c$ and $\tan\phi$ can be described using the following matrix:

$$A_{\mathrm{cr}} = \begin{bmatrix} 1 & \rho_{\mathrm{c}-\tan\phi} \\ \rho_{\mathrm{c}-\tan\phi} & 1 \end{bmatrix} \tag{9}$$

Since the cross-correlation matrix is positive definite, it can be decomposed into lower and upper triangular matrices using the Cholesky decomposition method given in the following equation:

$$A_{\mathrm{cr}} = \overline{QQ}^{\mathrm{T}} \tag{10}$$

Hence, the cross-correlated standard normal random fields for $c$ and $\tan\phi$ can be evaluated using the following expression:

$$\begin{pmatrix} G^{\mathrm{cr}}_{\ln\tan\overline{\phi}} \\ G^{cr}_{\ln\overline{c}} \end{pmatrix} = \begin{bmatrix} \overline{Q}_{11} & 0 \\ \overline{Q}_{21} & \overline{Q}_{22} \end{bmatrix} \begin{pmatrix} G_{\ln\tan\overline{\phi}} \\ G_{\ln\overline{c}} \end{pmatrix} \tag{11}$$

Here, $G_{\ln\overline{c}}$ is the auto-correlated standard normal field for cohesion which can be evaluated using the following equation:

$$G_{\ln\overline{c}} = \sum_{j=1}^{i} Q_{ij}\left(G_{\ln c}\right)_j,\ i = 1, 2, 3, \ldots, E_n \tag{12}$$

where $G_{\ln c}$ is the uncorrelated standard normal random field for cohesion with zero mean and unit standard deviation.

Since the lognormal distribution is considered for both $c$ and $\tan\phi$, the cross-correlated random fields for $c$ and $\phi$ can be evaluated using the following equations:

$$\phi(\xi) = \tan^{-1}[\exp(\mu_{\ln\tan\phi} + \sigma_{\ln\tan\phi} G^{cr}_{\ln\tan\overline{\phi}})] \tag{13}$$

$$c(\xi) = \tan^{-1}[\exp(\mu_{\ln c} + \sigma_{\ln c} G^{cr}_{\ln\overline{c}})] \tag{14}$$

The underlying normal distribution parameters for cohesion, i.e., $\mu_{\ln c}$ and $\sigma_{\ln c}$ are evaluated using the following transformations:

$$\sigma^2_{\ln c} = \ln\left(1 + \frac{\sigma^2_c}{\mu^2_c}\right) = \ln(1 + \mathrm{COV}^2_c) \tag{15}$$

$$\mu_{\ln c} = \ln\mu_c - \frac{1}{2}\sigma^2_{\ln c} \tag{16}$$

Figure 8a, b, and c illustrate the respective variations in $\mu_q$, $COV_q$, and $p_f$ with respect to $\theta_x/D = \theta_y/D$ for $\rho_{c\text{-}\tan\phi} = 0$ and $-0.5$ corresponding to constant values of $\phi = 30°$, $\psi = 0°$, $COV_{\tan\phi} = 20\%$, $\theta_z/D = 1$, and $D = 1$ m. The $\mu_q$ of the footing for $\rho_{c\text{-}\tan\phi} = -0.5$ shows higher values as compared to that for $\rho_{c\text{-}\tan\phi} = 0$, whereas the $COV_q$ of the footing for $\rho_{c\text{-}\tan\phi} = -0.5$ is observed to be less than that for $\rho_{c\text{-}\tan\phi} = 0$. The negative cross-correlation between $c$ and $\tan\phi$ indicates that the increase in the $\tan\phi$ value is associated with the decrease in $c$ value and vice versa. Hence, the averaging effect is present, which increases the $\mu_q$ and reduces the $COV_q$ for $\rho_{c\text{-}\tan\phi} = -0.5$. The $p_f$ of the system is also found to be smaller for $\rho_{c\text{-}\tan\phi} = -0.5$. However, the difference between $p_f$ for $\rho_{c\text{-}\tan\phi} = 0$ and $-0.5$ is only marginal for $\theta_x/D = \theta_y/D = 1.25$ and 2.5, and an observable difference is present for $\theta_x/D = \theta_y/D > 2.5$.

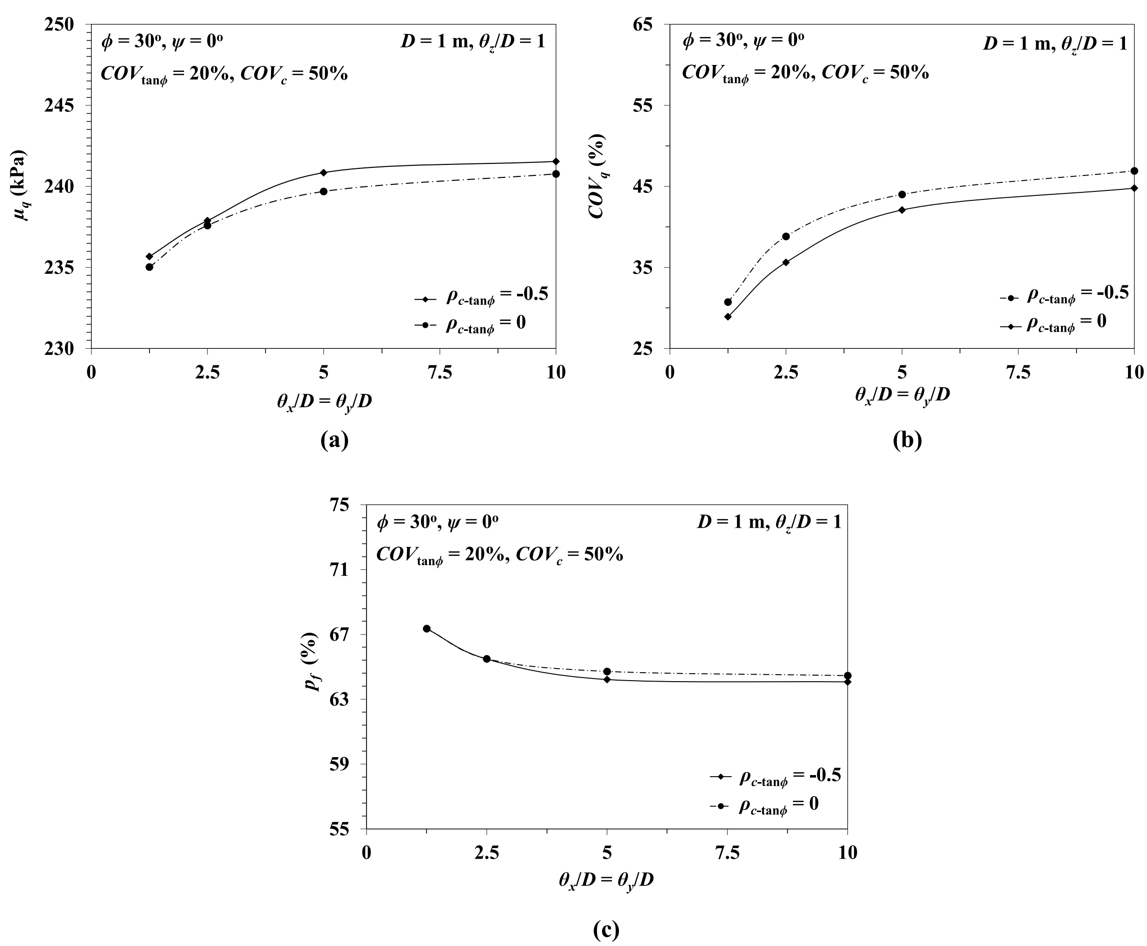


**Fig. 8** Variations in **a** $\mu_q$, **b** $COV_q$, and **c** $p_f$ of the circular footing with respect to $\theta_x/D = \theta_y/D$ for $\rho_{c\text{-}\tan\phi} = 0$ and $-0.5$

### 5.6 Failure Patterns

This study illustrates the failure mechanisms of the underlying spatially variable soil using the maximum shear strain rate contour plots. The comparisons of these failure patterns for different $\phi$ and $\psi$ corresponding to the constant values of $COV_{\tan\phi} = 10\%$, $\theta_x/D = \theta_y/D = 10$, $\theta_z/D = 1$, and $D = 1$ m are shown in Fig. 9. For a better

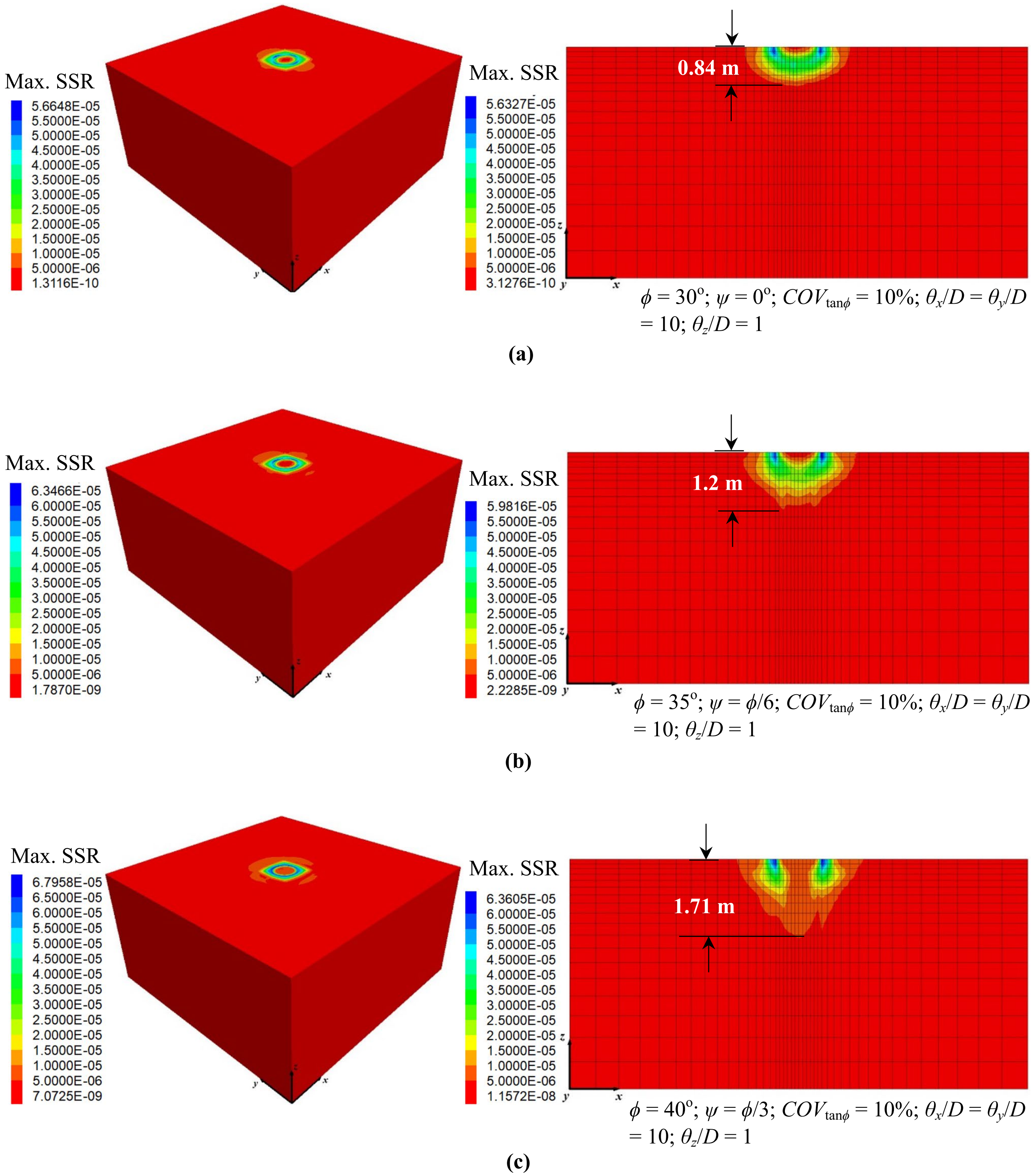


**Fig. 9** Maximum shear strain rate (Max. SSR) contour plots of the underlying spatially variable soil for **a** $\phi = 30°$, $\psi = 0°$ **b** $\phi = 35°$, $\psi = \phi/6$, and **c** $\phi = 40°$, $\psi = \phi/3$

understanding of the failure mechanism of the soil under the footing, the cross-sectional views of the failure patterns along the centroidal point of the footing in the $x$–$z$ plane are illustrated in Fig. 9. Despite having identical probabilistic statistics of underlying soil friction angle (for a particular value of $\phi$), different spatial orientations of $\phi$ are expected for different Monte Carlo realizations. Therefore, different bearing pressure–settlement responses are achieved for different realizations, where the bearing capacities reach their ultimate state for some of the realizations but they have yet to reach their limiting values for other realizations. Hence, the failure patterns illustrated in the figure correspond to a particular Monte Carlo realization. It is evident from the figure that the developed plastic regions are asymmetric for all the cases, as the generated $\phi$ (as well as $\psi$ except $\phi = 30°$) values are different at different spatial coordinates. It is also observed that the plastic regions are well developed and reach the ground surface for all $\phi$, indicating that the system is failing under the general shear failure mechanism in that particular realization. It is also evident from the figures that both $\phi$ and $\psi$ have profound effects on the failure pattern. With the increase in $\phi$ and $\psi$, the resistance offered by the underlying soil increases, and the $\phi$ and $\psi$ of the large volume of soil mass get mobilized during load transfer. Hence, the extent of the plastic zones in the depth direction as well as beyond the edge of the footing increase with the increase in $\phi$ and $\psi$. For example, the maximum depths of the bottom of the asymmetric failure zone (from the ground surface) are found to be 0.84 m, 1.2 m, and 1.71 m for (1) $\phi = 30°$, $\psi = 0°$, (2) $\phi = 35°$, $\psi = \phi/6$, and (3) $\phi = 40°$, $\psi = \phi/3$, respectively (for the particular realization). It is also observed that the maximum shear strain rate value increases with the increase in $\phi$ and $\psi$.

## 5.7 Variations in *CDF* and *PDF* for Different $COV_{\tan\phi}$, $\theta_x/D = \theta_y/D$, and $\theta_z/D$

The variations in *CDF* and *PDF* for different values of $COV_{\tan\phi}$ corresponding to the specific values of $\phi = 30°$, $\psi = 0°$, $\theta_x/D = \theta_y/D = 10$, $\theta_z/D = 1$, and $D = 1$ m are presented in Fig. 10a and d, respectively. It is clear from the *CDF* plot that for the lower values of the probabilistic $q_u$, the cumulative probability or the $p_f$ of the system increases with the increase in $COV_{\tan\phi}$. Similarly, at the $q_{ud}$, the $p_f$ also increases with the increase in $COV_{\tan\phi}$, although for higher values of $q_u$, $p_f$ decreases as the $COV_{\tan\phi}$ increases. The *PDF* plot clearly shows that the $q_u$ of the footing at the maximum probability of occurrence is less than the $q_{ud}$, and it decreases as the $COV_{\tan\phi}$ increases, suggesting that when the $COV_{\tan\phi}$ value increases, a significant reduction in $q_u$ occurs as compared to $q_{ud}$. It is also observed that the maximum probability of occurrence decreases as the $COV_{\tan\phi}$

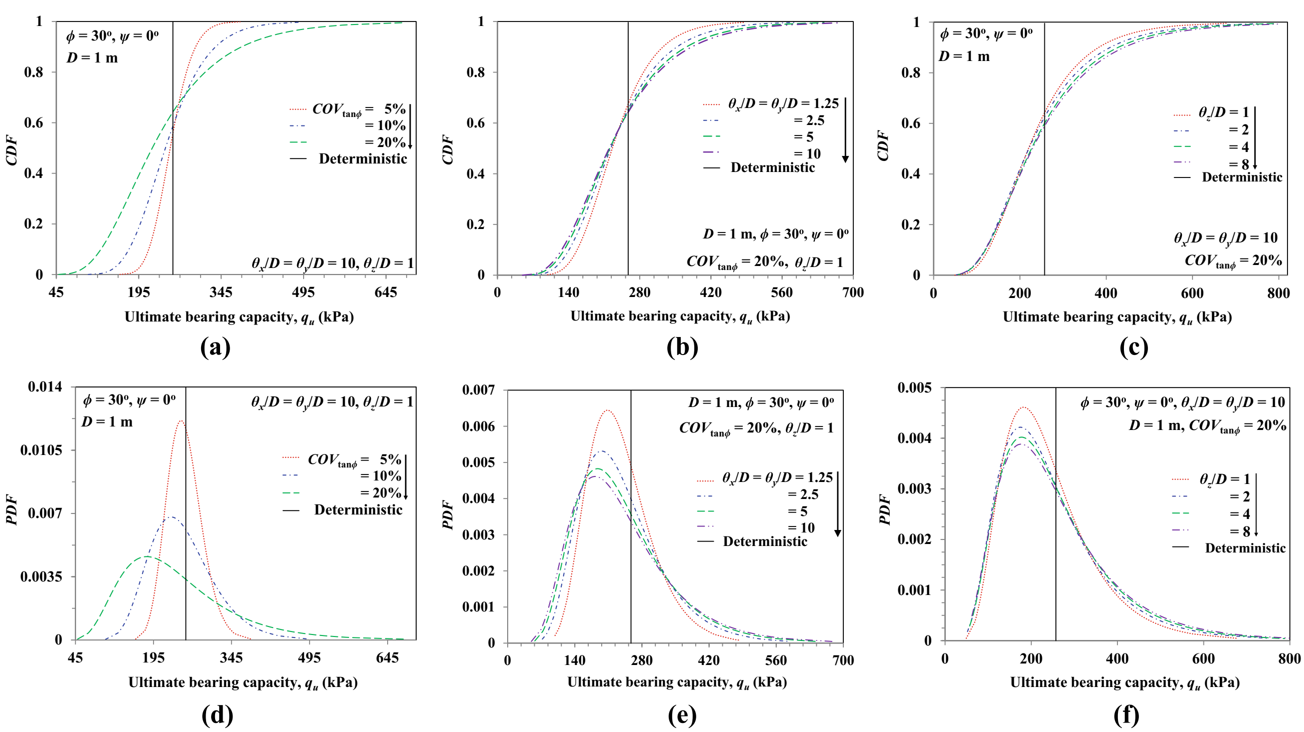


**Fig. 10** Variations in *CDF* of $q_u$ for different values of **a** $COV_{\tan\phi}$, **b** $\theta_x/D = \theta_y/D$, and **c** $\theta_z/D$; variations in *PDF* of $q_u$ for different values of **d** $COV_{\tan\phi}$, **e** $\theta_x/D = \theta_y/D$ and **f** $\theta_z/D$

increases, whereas the skewness of the *PDF* curve increases as the $COV_{\tan\phi}$ increases.

The variations in *CDF* and *PDF* for different $\theta_x/D=\theta_y/D$ corresponding to the particular values of $\phi=30°$, $\psi=0°$, $COV_{\tan\phi}=20\%$, $\theta_z/D=1$, and $D=1$ m are illustrated in Fig. 10b and e, respectively. Similarly, the variations in cumulative and probability density plots for different $\theta_z/D$ corresponding to the particular values of $\phi=30°$, $\psi=0°$, $COV_{\tan\phi}=20\%$, $\theta_x/D=\theta_y/D=10$, and $D=1$ m are represented in Fig. 10c and f, respectively. It is observed from the *CDF* plot that for the lower values of $q_u$, the cumulative probability increases as $\theta_x/D=\theta_y/D$ increase. However, at the $q_{ud}$ and for higher values of $q_u$, the cumulative probability decreases as $\theta_x/D=\theta_y/D$ increases. From the *PDF* plot, it can be clearly stated that the maximum probability of occurrence decreases as $\theta_x/D=\theta_y/D$ increases, and at $q_{ud}$, the probability of occurrence also decreases as $\theta_x/D=\theta_y/D$ increases. However, for the lower and higher values of $q_u$, the probability of occurrence increases as $\theta_x/D=\theta_y/D$ increases. A similar observation is observed for the variations in *CDF* and *PDF* with respect to $\theta_z/D$. However, for the lower values of $q_u$, the segments of *CDF* and *PDF* curves fall within a very tight band for $\theta_z/D$.

## 5.8 Variation in $p_f$ with Respect to *FOS*

The significance of probabilistic analyses is justified in the Introduction section as it helps calculate the $p_f$, which is found to be a more robust concept as compared to the *FOS*. However, $p_f$ and *FOS* are strongly correlated, which can be defined using the following expression:

$$p_{\mathrm{f}} = P(q_u < q_{\mathrm{ud}}/\mathrm{FOS}) = \Phi\left(\frac{\ln(q_{\mathrm{ud}}/\mathrm{FOS}) - \mu_{\ln q_u}}{\sigma_{\ln q_u}}\right) = \Phi(-\beta) \tag{17}$$

Figure 11a, b demonstrate the variations in $p_f$ with respect to the *FOS* for different $COV_{\tan\phi}$ and $\theta_x/D=\theta_y/D$, respectively. Both figures show a drastic reduction in $p_f$ with the increase in *FOS*. However, the observed trend is very obvious. For $COV_{\tan\phi}=5\%$, the $p_f$ of the system tends to zero

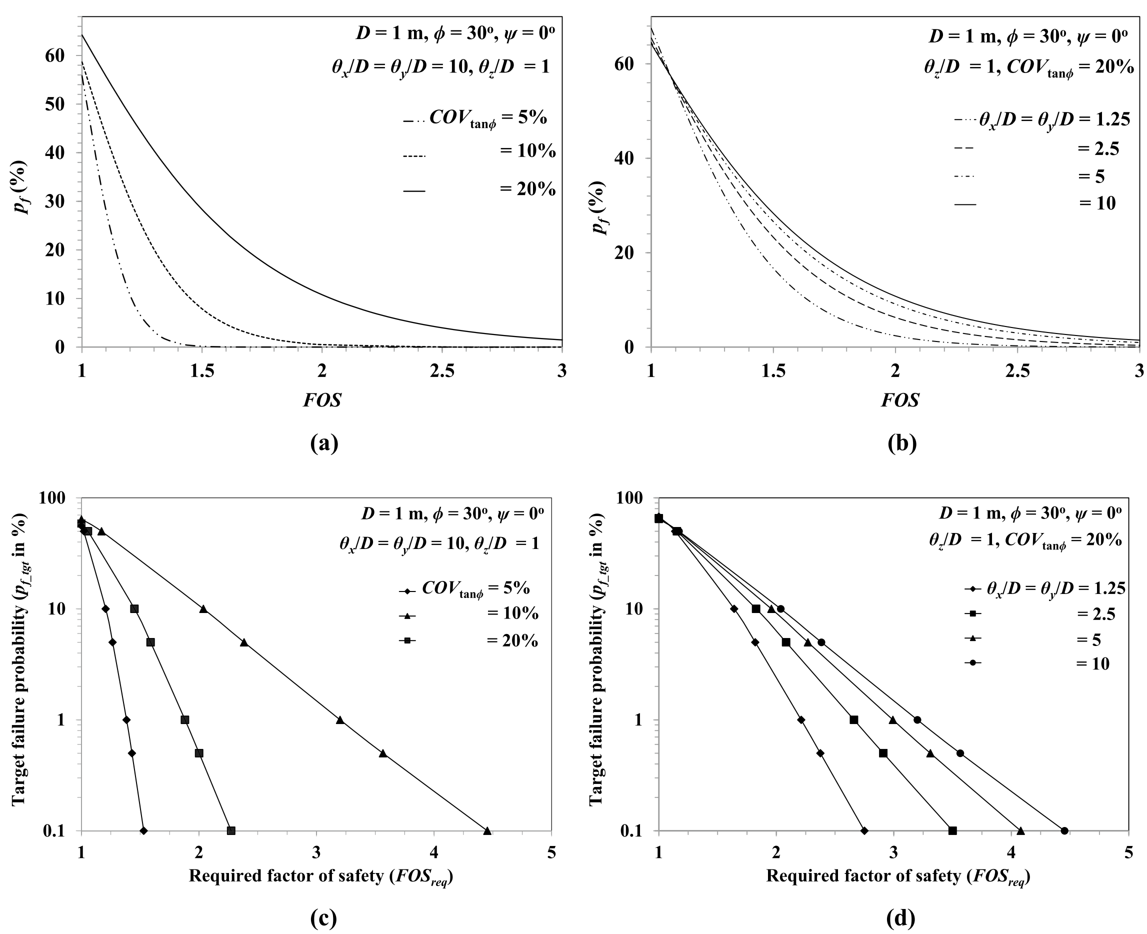


**Fig. 11** Variations in $p_f$ with respect to *FOS* for different values of **a** $COV_{\tan\phi}$, **b** $\theta_x/D=\theta_y/D$; variations in $p_{f\_tgt}$ with respect to $FOS_{req}$ for different values of **c** $COV_{\tan\phi}$, **d** $\theta_x/D=\theta_y/D$

when the $FOS$ approaches 1.7. Similarly, for $COV_{\tan\phi}=10\%$, the $p_f$ of the system tends to zero when the $FOS$ approaches 2.3, whereas for $COV_{\tan\phi}=20\%$, the system is not completely safe at $FOS=3$, as $p_f$ is found to be 1.5% at $FOS=3$. Hence, designing a typical footing considering $FOS=3$ can overestimate the allowable bearing capacity ($q_a$) for $COV_{\tan\phi}=5\%$ and 10%, whereas it can underestimate $q_a$ for $COV_{\tan\phi}=20\%$. It is found that for $FOS=1$, the $p_f$ of the system decreases as the $\theta_x/D=\theta_y/D$ increases, although the variation is very small. However, for the $FOS$ values $\geq 1.1$, $p_f$ increases as $\theta_x/D=\theta_y/D$ increases. The significant variation in $p_f$ for different $\theta_x/D=\theta_y/D$ is observed as the $FOS$ increases from 1.3 to 2.5. As the $FOS$ increases beyond 2.5, the variation in $p_f$ for different $\theta_x/D=\theta_y/D$ decreases. It is also observed that for $\theta_x/D=\theta_y/D=1.25$, $p_f$ tends to zero when the $FOS$ approaches 2.6, whereas the system $p_f$ is found to be 1.5% for $\theta_x/D=\theta_y/D=10$ at $FOS=3$. Hence, at $FOS=3$, $q_a$ is slightly overestimated for $\theta_x/D=\theta_y/D=1.25$, whereas it is underestimated for $\theta_x/D=\theta_y/D=10$. Based on these observations, Fig. 11c and d are plotted, estimating the required factor of safety ($FOS_{req}$) to achieve a specific target failure probability ($p_{f\_tgt}$). The $FOS_{req}$ corresponding to a specific $p_{f\_tgt}$ can be evaluated by rearranging Eq. (17) as follows:

$$\mathrm{FOS_{req}} = \frac{q_{\mathrm{ud}}}{\exp[\mu_{\ln q_u} + \sigma_{\ln q_u}\{\Phi^{-1}(p_{\mathrm{f\_tgt}})\}]} \tag{18}$$

Figure 11c, d represents $p_{f\_tgt}$ versus $FOS_{req}$ for different $COV_{\tan\phi}$ and $\theta_x/D=\theta_y/D$, respectively. For a given $p_{f\_tgt}$ (say $p_{f\_tgt}=0.1\%$), the $FOS_{req}$ increases with the increase in $COV_{\tan\phi}$. A similar trend is observed for $\theta_x/D=\theta_y/D$. For example, $FOS_{req}$ increases from 1.53 to 4.45 as the $COV_{\tan\phi}$ increases from 5 to 20% to achieve a $p_{f\_tgt}=0.1\%$ for the particular values of $\phi=30°$, $\psi=0°$, $\theta_x/D=\theta_y/D=10$, $\theta_z/D=1$, and $D=1$ m. Similarly, the $FOS_{req}$ is observed to increase from 2.75 to 4.45 as $\theta_x/D=\theta_y/D$ increases from 1.25 to 10 for the particular values of $\phi=30°$, $COV_{\tan\phi}=20\%$, $\theta_z/D=1$, and $D=1$ m.

### 5.9 Variations in $q_{ad}$ of Footing for Different $\beta$, $COV_{\tan\phi}$, and $\theta_x/D=\theta_y/D$

The present study also attempts to evaluate the $q_{ad}$ of the footing by modifying Eq. (8) as follows:

$$\Phi\left(\frac{\ln(q_{\mathrm{ad}}) - \mu_{\ln q_{\mathrm{u}}}}{\sigma_{\ln q_{\mathrm{u}}}}\right) = \Phi(-\beta) \tag{19}$$

By rearranging the above equation, the $q_{ad}$ of the footing can be obtained directly as follows:

$$q_{\mathrm{ad}} = \exp(\mu_{\ln q_u} - \beta\sigma_{\ln q_u}) \tag{20}$$

Four different reliability indices are used in this study to obtain $q_{ad}$: (1) $\beta=3.0902$, corresponding to the target failure probability ($p_{f\_tgt}$) of 0.1%; (2) $\beta=3.8$, which corresponds to the RC2 reliability class structures (residential and office buildings and their typical foundations) having medium consequences of failure, and 50 years of design working life (CEN 2002); (3) $\beta=3.0$ for the average performance and (4)

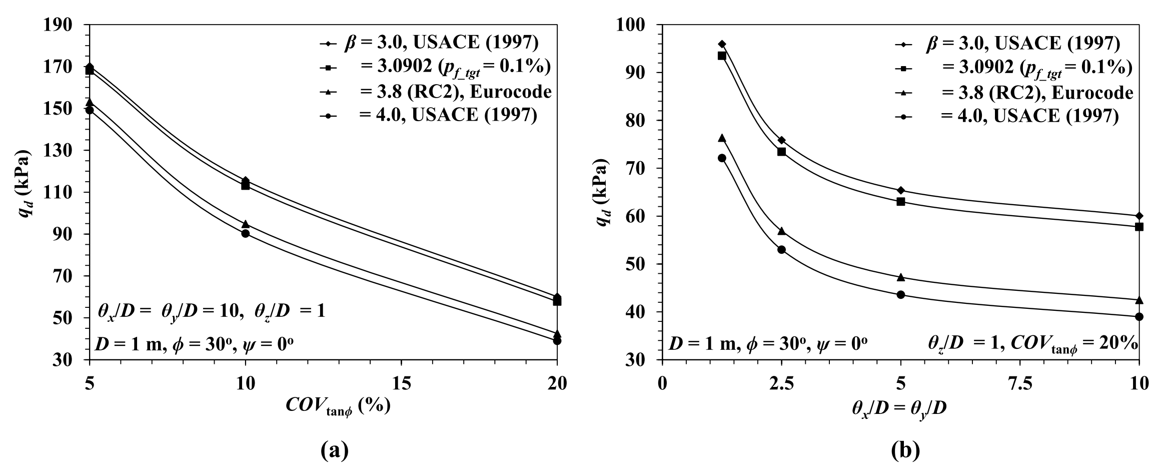


**Fig. 12** Variations in $q_{ad}$ of the footing with respect to $\beta$ for different values of **a** $COV_{\tan\phi}$, **b** $\theta_x/D=\theta_y/D$

$\beta = 4.0$ for the good performance of the geotechnical structures provided by USACE (1997). The variations in $q_{ad}$ with respect to $\beta$ for different $COV_{\tan\phi}$ and $\theta_x/D = \theta_y/D$ are shown in Fig. 12a and b, respectively. As illustrated in the figures, the $q_{ad}$ decreases with the increase in $\beta$. Similarly, a drastic decrease in $q_{ad}$ is also seen with the increase in $COV_{\tan\phi}$ for the constant values of $\beta$ and $\theta_x/D = \theta_y/D$ (Fig. 12a). Likewise, a lower value of $\theta_x/D = \theta_y/D$ provides a higher value of $q_{ad}$, whereas for higher values of $\theta_x/D = \theta_y/D$, the $q_{ad}$ obtained is quite low (Fig. 12b). However, the $q_{ad}$ values approach stable solutions as $\theta_x/D = \theta_y/D$ increases. Kawa and Pula (2020) observed a similar trend.

## 6 Remarks

The present study primarily estimates the probabilistic bearing capacity of circular footing. However, while estimating the bearing capacity of the footing, it is also necessary to calculate the probabilistic allowable settlement of the foundation. For this reason, the elastic modulus ($E$) and Poisson's ratio ($\upsilon$) of the foundation soil need to be considered as the random field. Hence, the cross-correlated random fields for the elastic modulus ($E$) and Poisson's ratio ($\upsilon$) are generated, and the probabilistic allowable foundation settlement ($\delta_{all}$) is evaluated corresponding to an allowable bearing pressure ($q_a$) of 150 kPa, considering both $E$ and $\upsilon$ as lognormally distributed, with $\mu_E = 30$ MPa, $\mu_\upsilon = 0.3$, $COV_E = 30\%$, $COV_\upsilon = 5\%$, and $\rho_{E\text{-}\upsilon} = -0.5$ (following Johari and Sabzi 2017). As a representative case, the $CDF$ and histogram fit of probabilistic allowable settlements are plotted for $\theta_x/D = \theta_y/D = 10$ and $\theta_z/D = 1$ (Fig. 13). It is clear from Fig. 13 that the probabilistic allowable settlement of the foundation follows the Weibull distribution. The distribution of the probabilistic allowable settlement is further confirmed using the Kolmogorov–Smirnov goodness-of-fit test. It is also found that the obtained absolute difference between the actual distribution and the theoretical Weibull distribution is well below the critical value of the difference for the given significance levels (i.e., $\alpha = 1\%$, 5%, and 20%). Hence, the assumed theoretical distribution is acceptable at those given significance levels, and the $p_f$ of the system in terms of the allowable settlement can be estimated as the probability for which the evaluated $\delta_{all}$ is greater than the deterministic allowable settlement ($\delta_{all\_det}$), as follows:

$$p_f = P(\delta_{\text{all}} > \delta_{\text{all\_det}}) = 1 - P(\delta_{\text{all}} \le \delta_{\text{all\_det}}) = 1 - \left(1 - e^{-\left(\frac{\delta_{\text{all\_det}}}{A}\right)^B}\right) = e^{-\left(\frac{\delta_{\text{all\_det}}}{A}\right)^B} \tag{21}$$

In the above equation, $A$ and $B$ denote the respective scale and shape parameters for the Weibull distribution.

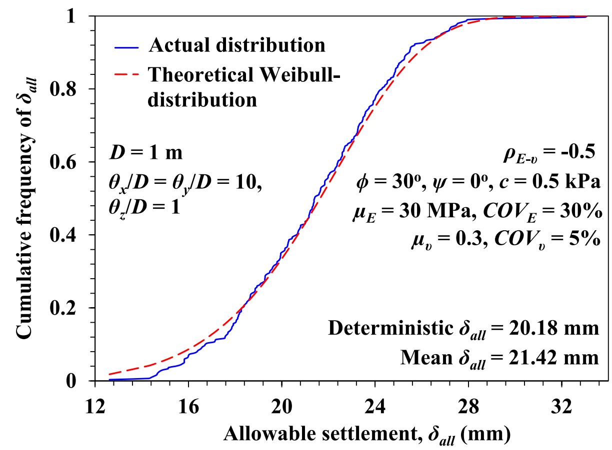


(a)

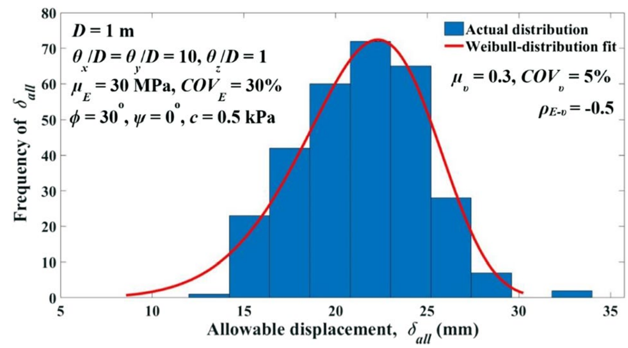


(b)

**Fig. 13** **a** Comparison of actual distribution with the assumed theoretical Weibull distribution of $\delta_{all}$, **b** histogram of $\delta_{all}$ with the Weibull-distribution fit for $D = 1$ m, $\phi = 30°$, $\psi = 0°$, $c = 0.5$ kPa, $\mu_E = 30$ MPa, $\mu_\upsilon = 0.3$, $COV_E = 30\%$, $COV_\upsilon = 5\%$, $\rho_{E\text{-}\upsilon} = -0.5$, $\theta_x/D = \theta_y/D = 10$, and $\theta_z/D = 1$

The variations in the mean, coefficient of variation of allowable settlement ($\mu\delta_{all}$ and $COV\_\delta_{all}$), and the failure probability ($p_f$) of the footing in terms of allowable settlement for different $\theta_x/D = \theta_y/D$ are presented in Fig. 14a, b, and c, respectively. The $\mu\delta_{all}$ of the footing decreases with the increase in $\theta_x/D = \theta_y/D$. However, the variation in $\mu\delta_{all}$ is very insignificant beyond $\theta_x/D = \theta_y/D = 2.5$. In contrast to $\mu\delta_{all}$, the $COV\_\delta_{all}$ increases with the increase in $\theta_x/D = \theta_y/D$ because of the averaging effect. The failure probability of the system is found to be decreasing with the increase in $\theta_x/D = \theta_y/D$.

## 7 Conclusions

The present study explores the spatial variability effect of soil friction and dilation angles on the bearing capacity of a three-dimensional circular surface footing resting on sandy soil. Deterministic analyses are carried out for

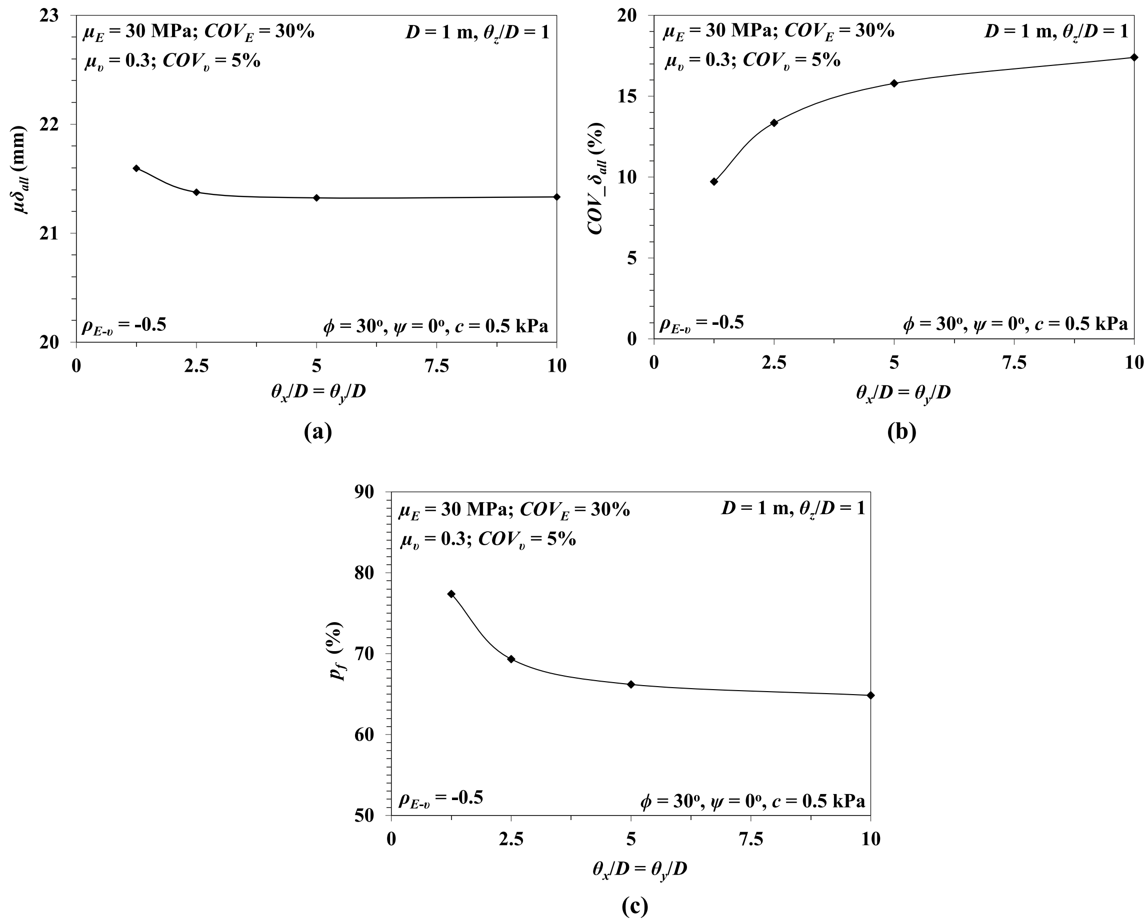


**Fig. 14** Variations in **a** $\mu\delta_{all}$, **b** $COV\_\delta_{all}$, and **c** $p_f$ of the circular footing with respect to $\theta_x/D=\theta_y/D$ for $D=1$ m, $\theta_z/D=1$, $\phi=30°$, $\psi=0°$, $c=0.5$ kPa

three different combinations of $\phi$ and $\psi$ ($\phi=30°$, $\psi=0°$; $\phi=35°$, $\psi=\phi/6$; and $\phi=40°$, $\psi=\phi/3$) and three different $D$ ($D=0.5$ m, 1 m, and 2 m). In the case of probabilistic analyses, the tan$\phi$ is assumed to be lognormally distributed instead of $\phi$. The main focus of the study is to investigate the effect of $\theta_x/D=\theta_y/D$ on the $\mu_q$ and $p_f$ of the system for different values of $\phi$, $\psi$, $COV_{\tan\phi}$, $\theta_z/D$, and $D$. The probabilistic allowable settlement of the footing corresponding to the allowable bearing pressure of 150 kPa is also evaluated considering the $E$ and $\upsilon$ as the lognormally distributed cross-correlated random fields. The essential conclusive remarks drawn from the present study are listed below:

(1) Higher values of $\phi$, $\psi$, $COV_{\tan\phi}$, and $D$ have a notable impact on the $\mu_q$ and the $p_f$ of the system. $\phi=40°$, $\psi=\phi/3$ (for $D=1$ m, $COV_{\tan\phi}=20\%$, $\theta_z/D=1$, and $FOS=1$) shows the opposite trend of $\mu_q$ (with respect to $\theta_x/D=\theta_y/D$) which is observed for $\phi=30°$, $\psi=0°$ and $\phi=35°$, $\psi=\phi/6$. Similarly, $D=2$ m (for $\phi=30°$, $\psi=0°$, $COV_{\tan\phi}=20\%$, $\theta_z/D=1$, and $FOS=1$) shows the opposite trend of $\mu_q$ which is observed for $D=0.5$ m and 1 m. Additionally, $\phi=40°$, $\psi=\phi/3$, and $D=2$ m give the highest value of $p_f$ as compared to the other cases.

(2) The negative cross-correlation between $c$ and tan$\phi$ shows higher values of $\mu_q$ and lower values of $COV_q$ and $p_f$ than the case without cross-correlation, irrespective of the change in $\theta_x/D=\theta_y/D$. In the case of $p_f$, the change in it is only marginal up to $\theta_x/D=\theta_y/D=2.5$, beyond which there is an observable difference.

(3) The use of the $FOS$ concept may overestimate the $q_a$ of the footing for lower values of $COV_{\tan\phi}$, whereas it may underestimate the $q_a$ for higher values of $COV_{\tan\phi}$. Similarly, the $q_a$ gets overestimated for lower $\theta_x/D=\theta_y/D$ and underestimated for higher $\theta_x/D=\theta_y/D$.

(4) Estimating the $FOS_{req}$ is essential, as higher values of $FOS$ do not ensure that the system is entirely safe

against failure. Hence, the $FOS_{req}$ is calculated based on the fundamental concept of failure probability to achieve a target $p_f$ of the system. It is found that to achieve a $p_{f\_tgt}$ of 0.1%, the $FOS_{req}$ increases as the $COV_{\tan\phi}$ and $\theta_x/D = \theta_y/D$ increase.

(5) The $q_{ad}$ of the footing decreases significantly as $\beta$, $COV_{\tan\phi}$, and $\theta_x/D = \theta_y/D$ increase. However, the variation in $q_{ad}$ decreases as $\theta_x/D = \theta_y/D$ approaches a higher value.

(6) The probabilistic allowable settlement ($\delta_{all}$) is observed to follow the Weibull distribution. The $\mu\delta_{all}$ and $p_f$ associated with the allowable settlement is found to decrease with the increase in $\theta_x/D = \theta_y/D$, whereas $COV\_\delta_{all}$ increases with the increase in $\theta_x/D = \theta_y/D$.

(7) The primary focus of the present study is on estimating the probabilistic bearing capacity of circular footing. The probabilistic allowable settlement of the footing corresponding to a specific allowable bearing pressure is also evaluated. However, it is also essential to evaluate the probabilistic allowable differential settlement of two closely spaced circular footings, which is beyond the scope of the study and can be considered in a future study.

The trend of using the spatial variability concept in the geotechnical fields has grown rapidly over the past few decades. The present analysis of the probabilistic bearing capacity of circular footing, considering the inherent spatial variability of the soil shear strength parameters under vertical loading, provides a general perspective of the problem. The risk associated with the potential failure of the footing is also discussed in the study. Hence, the authors hope the present study will help engineers working on this type of problem.

## Declarations

**Conflict of interest** The authors declare that there are no competing interests.

## References


Ahmed A, Soubra A-H (2014) Reliability analyses at ultimate and serviceability limit states of obliquely loaded circular foundations. Geotech Geol Eng 32(4):729–738. https://doi.org/10.1007/s10706-014-9750-y

Al-Bittar T, Soubra A-H (2014) Combined use of the sparse polynomial chaos expansion and the global sensitivity analysis for the probabilistic analysis of shallow foundations resting on a 3D random soil. In: Deodatis G, Ellingwood BR, Frangopol DM (eds) Safety, Reliability, Risk and Life-Cycle Performance of Structures and Infrastructures. CRC Press, Boca Raton, pp 3261–3268

CEN (European Committee for Standardization) (2002) Eurocode - basis of structural design. EN 1990, Brussels, Belgium

CEN (European Committee for Standardization) (2013) geotechnical design worked examples. Eurocode 7, Ispra, Italy

Cheng H, Chen J, Chen R, Chen G, Zhong Y (2018) Risk assessment of slope failure considering the variability in soil properties. Comput Geotech 103:61–72. https://doi.org/10.1016/j.compgeo.2018.07.006

Cherubini C (2000) Reliability evaluation of shallow foundation bearing capacity on $c'$, $\phi'$ soils. Can Geotech J 37(1):264–269. https://doi.org/10.1139/t99-096

Cho SE, Park HC (2010) Effect of spatial variability of cross-correlated soil properties on bearing capacity of strip footing. Int J Numer Anal Methods Geomech 34(1):1–26. https://doi.org/10.1002/nag.791

Choudhuri K, Chakraborty D (2021) Probabilistic bearing capacity of a pavement resting on fibre reinforced embankment considering soil spatial variability. Front Built Environ 7:628016. https://doi.org/10.3389/fbuil.2021.628016

Choudhuri K, Chakraborty D (2022) Probabilistic analyses of three-dimensional circular footing resting on two-layer $c$–$\phi$ soil system considering soil spatial variability. Acta Geotech. https://doi.org/10.1007/s11440-022-01701-7

Chwała M, Kawa M (2021) Random failure mechanism method for assessment of working platform bearing capacity with a linear trend in undrained shear strength. J Rock Mech Geotech Eng 13(6):1513–1530. https://doi.org/10.1016/j.jrmge.2021.06.004

Erickson HL, Drescher A (2002) Bearing capacity of circular footings. J Geotech Geoenviron Eng 128(1):38–43. https://doi.org/10.1061/(ASCE)1090-0241(2002)128:1(38)

Fenton GA, Griffiths DV (2002) Probabilistic foundation settlement on spatially random soil. J Geotech Geoenviron Eng 128(5):381–390. https://doi.org/10.1061/(ASCE)1090-0241(2002)128:5(381)

Fenton GA, Griffiths DV (2003) Bearing capacity prediction of spatially random $c$ - $\phi$ soils. Can Geotech J 40(1):54–65. https://doi.org/10.1139/t02-086

Fenton GA, Griffiths DV (2005) Three-dimensional probabilistic foundation settlement. J Geotech Geoenviron Eng 131(2):232–239. https://doi.org/10.1061/(ASCE)1090-0241(2005)131:2(232)

Gong W, Wang L, Khoshnevisan S, Juang CH, Huang H, Zhang J (2015) Robust geotechnical design of earth slopes using fuzzy sets. J Geotech Geoenviron Eng 141(1):04014084. https://doi.org/10.1061/(ASCE)GT.1943-5606.0001196

Griffiths DV, Fenton GA (2004) Probabilistic slope stability analysis by finite elements. J Geotech Geoenviron Eng 130(5):507–518. https://doi.org/10.1061/(ASCE)1090-0241(2004)130:5(507)

Griffiths DV, Fenton GA, Manoharan N (2002) Bearing capacity of rough rigid strip footing on cohesive soil: Probabilistic study. J Geotech Geoenviron Eng 128(9):743–755. https://doi.org/10.1061/(ASCE)1090-0241(2002)128:9(743)

Griffiths DV, Fenton GA, Manoharan N (2006) Undrained bearing capacity of two-strip footings. Int J Geomech 6(6):421–427. https://doi.org/10.1061/(ASCE)1532-3641(2006)6:6(421)

Griffiths DV, Huang J, Fenton GA (2011) Probabilistic infinite slope analysis. Comput Geotech 38(4):577–584. https://doi.org/10.1016/j.compgeo.2011.03.006

Haldar S, Sivakumar Babu GL (2008) Effect of soil spatial variability on the response of laterally loaded pile in undrained clay. Comput Geotech 35(4):537–547. https://doi.org/10.1016/j.compgeo.2007.10.004

Halder K, Chakraborty D (2020) Influence of soil spatial variability on the response of strip footing on geocell-reinforced slope. Comput Geotech 122:103533. https://doi.org/10.1016/j.compgeo.2020.103533

Itasca Consulting Group, FLAC$^{3D}$ (2012) Fast Lagrangian analysis of continua, version 5.01: user's and theory manuals. Minneapolis: Itasca Consulting Group Inc, USA

Jamshidi Chenari R, Mahigir A (2014) The effect of spatial variability and anisotropy of soils on bearing capacity of shallow foundations. Civ Eng Infrastruct J 47(2):199–213. https://doi.org/10.7508/ceij.2014.02.004

Johari A, Sabzi A (2017) Reliability analysis of foundation settlement by stochastic response surface and random finite element method. Sci Iran 24(6):2741–2751

Johari A, Hosseini SM, Keshavarz A (2017) Reliability analysis of seismic bearing capacity of strip footing by stochastic slip lines method. Comput Geotech 91:203–217. https://doi.org/10.1016/j.compgeo.2017.07.019

Johari A, Sabzi A, Gholaminejad A (2019) Reliability analysis of differential settlement of strip footings by stochastic response surface method. Iran J Sci Technol - Trans Civ Eng 43:37–48. https://doi.org/10.1007/s40996-018-0114-3

Kasama K, Whittle AJ (2016) Effect of spatial variability on the slope stability using random field numerical limit analyses. Georisk Assess Manag Risk Syst GeoHazards 10(1):42–54. https://doi.org/10.1080/17499518.2015.1077973

Kawa M, Puła W (2020) 3D bearing capacity probabilistic analyses of footings on spatially variable *c*–*ϕ* soil. Acta Geotech 15(6):1453–1466. https://doi.org/10.1007/s11440-019-00853-3

Krishnan K, Chakraborty D (2022) Probabilistic study on the bearing capacity of strip footing subjected to combined effect of inclined and eccentric loads. Comput Geotech 141:104505

Loukidis D, Salgado R (2009) Bearing capacity of strip and circular footings in sand using finite elements. Comput Geotech 36(5):871–879. https://doi.org/10.1016/j.compgeo.2009.01.012

Luo N, Luo Z (2022) Risk assessment of footings on slopes in spatially variable soils considering random field rotation. ASCE ASME J Risk Uncertain Eng Syst A Civ 8(3):1–10. https://doi.org/10.1061/AJRUA6.0001252

Luo Z, Atamturktur S, Cai Y, Juang CH (2012) Reliability analysis of basal-heave in a braced excavation in a 2-D random field. Comput Geotech 39:27–37. https://doi.org/10.1016/j.compgeo.2011.08.005

Manoharan N, Dasgupta SP (1995) Bearing capacity of surface footings by finite elements. Comput Struct 54(4):563–586. https://doi.org/10.1016/0045-7949(94)00381-C

Massey FJ Jr (1951) The Kolmogorov-Smirnov test for goodness of fit. J Am Stat Assoc 46(253):68–78. https://doi.org/10.1080/01621459.1951.10500769

Mollon G, Dias D, Soubra A-H (2009) Probabilistic analysis of circular tunnels in homogeneous soil using response surface methodology. J Geotech Geoenviron Eng 135(9):1314–1325. https://doi.org/10.1061/(ASCE)GT.1943-5606.0000060

Nazeeh KM, Sivakumar Babu GL (2021) Reliability-based robust design of raft foundation and effect of spatial variability. ASCE ASME J Risk Uncertain Eng Syst A Civ 7(4):1–10. https://doi.org/10.1061/AJRUA6.0001171

Ornek M, Laman M, Demir A, Yildiz A (2012) Numerical analysis of circular footings on natural clay stabilized with a granular fill. Acta Geotech Slov 9(1):61–75

Phoon K-K, Kulhawy FH (1999) Characterization of geotechnical variability. Can Geotech J 36(4):612–624. https://doi.org/10.1139/t99-038

Simões JT, Neves LC, Antão AN, Guerra NMC (2013) Probabilistic analysis of bearing capacity of shallow foundations using 3D limit analyses. Int J Comput Methods 11(02):1342008. https://doi.org/10.1142/S0219876213420085

Sloan SW (2013) Geotechnical Stability Analysis Géotechnique 7:531–572. https://doi.org/10.1680/geot.12.RL.001

The MathWorks Inc. (2020) MATLAB (R2020b), version 9.9. Massachusetts, United States.

U.S. Army Corps of Engineers (USACE) (1997) Engineering and design: Introduction to probability and reliability methods for use in geotechnical engineering. Eng. Circ. 1110–2–547, U.S. Dept. of the Army, Washington, DC

Vanmarcke EH (1983) Random fields: Analysis and synthesis. MIT Press, Cambridge, MA

Wu Y, Zhou X, Gao Y, Zhang L, Yang J (2019) Effect of soil variability on bearing capacity accounting for non-stationary characteristics of undrained shear strength. Comput Geotech 110:199–210. https://doi.org/10.1016/j.compgeo.2019.02.0